



Excellent disinfection and fluoride removal using bifunctional nanocomposite

Ankita Dhillon^a, Sapna^a, B.L. Choudhary^b, Dinesh Kumar^{c,*}, Surendra Prasad^{d,*}

^a Department of Chemistry, Banasthali University, Rajasthan 304022, India

^b Department of Physics, University of Rajasthan, Jaipur 302004, India

^c School of Chemical Sciences, Central University of Gujarat, Gandhinagar 382030, India

^d School of Biological and Chemical Sciences, Faculty of Science, Technology and Environment, The University of the South Pacific, Private Mail Bag, Suva, Fiji

ARTICLE INFO

Keywords:

Nanocomposite
Decontamination
Fluoride removal
Disinfection
Reusability
Adsorption

ABSTRACT

Bacterium (*Staphylococcus aureus*) and fluoride are considered as acute dental infectants. Simultaneous bacterial and fluoride decontamination for healthy teeth is therefore of high priorities. Hence, we have fabricated a Ca–Ce nanocomposite (NC) for dual decontamination of bacteria and fluoride from drinking water. The antibacterial activities were performed against *Escherichia coli* (*E. coli*) and *Staphylococcus aureus* (*S. aureus*) using bacterial growth curves based on optical density and colony growth using the well diffusion method. The dose-dependent antibacterial activity showed 50% bacterial inhibition (IC₅₀) at 31.5 and 27.0 μg mL⁻¹ Ca–Ce NC concentrations for *E. coli* and *S. aureus* cells, respectively within 4 h of exposure. The mechanism of antibacterial action was evaluated using membrane protein leakage studies as well as dehydrogenase enzyme activity analysis of treated bacterial cells coupled with scanning electron microscopy (SEM) analysis. The fluoride adsorption mechanism was confirmed using FTIR and X-ray photoelectron spectroscopy (XPS) studies which supported the involvement of –OH groups on Ca and Ce ions where Ce–OH was the preferred adsorption site even at low Ce concentration in the nanocomposite as Ca:Ce ≈ 2:1. The prepared Ca–Ce NC proved to be very promising for water purification.

1. Introduction

Bacteria and fluoride are common drinking water contaminants. Bacterial infections, especially by Gram-positive *Staphylococcus aureus* can cause severe oral infections [1] and has been detected in some acute dentalveolar infections, such as a dental abscess [2–4]. Among Gram-negative bacteria, *Escherichia coli* has been known to cause frequent infections due to biofilm formation which shows higher resistance to antibiotics and disinfecting agents [5–7]. Similarly, fluoride is a serious oral infectant that has detrimental effects and causes dental fluorosis if present at a concentration greater than World Health Organization (WHO) limits i.e. 1.5 mg L⁻¹ [8,9]. Thus, fabrication of novel antibacterial, as well as fluoride decontamination agents, is of great interest for today's generation. Organic antibacterial agents are generally sensitive to high temperature and pressure [10–12]. Therefore, there has been an increasing interest in inorganic disinfectants due to their better actions. Thus, few metal oxides nanomaterials, like CuO, MgO, and CaO have been extensively studied as antibacterial agents due to their inherent characteristics like highly stable, non-hazardous, small size and high specific surface area [13–16]. Antibacterial activities of cerium oxide and calcium oxide have also been studied by few

researchers but have shown lower bactericidal properties and their mechanism is still unclear [17,18].

Among various fluoride removal techniques [19–21] adsorptive removal using metal oxide based adsorbents has been the principal method for defluoridation of water [22–24]. Although several mixed metal oxides adsorbents have been reported, detailed studies concerning the preferential adsorption sites and quantitative ligand exchange relationship has still not been clearly understood. The literature survey revealed that few metal oxides based bacterial disinfectants and fluoride decontaminants have been developed, but very few reports are available for the simultaneous decontamination of bacteria as well as fluoride from drinking water [25,26]. Thus, this paper reports an efficient method for bacterial and fluoride decontamination from drinking water by our indigenously developed Ca–Ce mixed oxides nanocomposite (NC).

2. Materials and methods

2.1. Materials

CaSO₄·70 and (NH₄)₂[Ce(NO₃)₆] used in the synthesis of Ca–Ce NC

* Corresponding authors.

E-mail addresses: dinesh.kumar@cug.ac.in (D. Kumar), prasad_su@usp.ac.fj (S. Prasad).

were of analytical grade. Sodium fluoride (NaF), sodium chloride (NaCl), sodium carbonate (Na_2CO_3), sodium phosphate (Na_3PO_4), sodium nitrate (NaNO_3) and anhydrous sodium sulfate (Na_2SO_4) required during coexisting anions study were also analytical grade reagents. Most of the chemicals were procured from Sigma-Aldrich. The Gram-negative *E. coli* bacterial strain (MTCC-294) and Gram-positive *S. aureus* bacterial strain (MTCC-3160) used in this study were obtained from the Institute of Microbial Technology, Chandigarh, India.

2.2. Synthesis of nanocomposite and antibacterial analysis

0.1 M solution of $\text{CaSO}_4 \cdot 7\text{H}_2\text{O}$ and 0.1 M solution of $(\text{NH}_4)_2[\text{Ce}(\text{NO}_3)_6]$ were prepared separately by dissolving their calculated amounts in distilled deionized water (DDW). The solutions were mixed and 2 M NaOH solution steadily added with constant stirring until the pH reached to 8.5 ± 0.2 . The precipitate obtained was repeatedly centrifuged, filtrated, washed with DDW and ethanol, and finally dried in a drying oven at 100°C and ground to a fine powder. Furthermore, the adsorbent was activated by calcining in a muffle furnace up to 600°C . The adsorbent was optimized at different Ca/Ce molar ratios and calcination temperature to attain maximum fluoride removal efficiency.

The detailed descriptions of the assessment of IC_{50} values of Ca-Ce NC using Gram-negative and Gram-positive bacteria and well diffusion method have been provided in the ESI file.

2.3. Characterization of nanocomposite

2.3.1. BET analysis

Brunauer, Emmett and Teller (BET) analysis was used to determine the specific surface areas of adsorbent by nitrogen monolayer adsorption measured as a function of relative pressure using a fully automated analyzer, model Nova 2000e (Quantachrome Instruments Limited, USA). At one of the degassing stations 0.30 g of the powder sample was placed in the sample cell and allowed to degas for 3 h at 300°C in a vacuum degassing mode. The specific surface area of Ca-Ce NC was estimated using multipoint BET equation in the P/P_0 range of 0.07–0.30.

2.3.2. Zeta potential

The sample was prepared by dissolving 0.30 g of Ca-Ce NC i.e. nano-adsorbent into 250 mL of deionized water and 0.1 M NaCl and the pH of the solution was varied from 3 to 12 with the help of 0.1 M NaOH or 0.1 M HCl. The obtained suspensions were stirred at room temperature, and the zeta potential was measured with a Zetasizer Nano ZS (Malvern Instrument, UK).

2.3.3. Field emission scanning electron microscopy and XRD studies

The morphology of the Ca-Ce nano-adsorbent surfaces was characterized using a field emission scanning electron microscope (FESEM, MIRA3 TESCAN). Energy dispersive X-ray (EDX) analysis of the samples was carried out to determine the mean element proportions of the sample on an Oxford Instrument INCA attached to the FESEM. For EDX analysis an accelerating voltage of 30 kV was used with an acquisition time of about 1 min. An extremely thin vacuum evaporated carbon coating of samples was done to improve the conductivity of the samples.

The crystal structural analysis of nanocomposite was carried out using X-ray diffractometer with Cu-K α radiation over a range of 10 – 70° at a scan speed of 5°min^{-1} .

2.3.4. FTIR and XPS study

The Fourier transform infrared spectroscopy (FTIR) spectra were recorded in the range of 4000 – 400cm^{-1} by using an FTIR spectrophotometer (Agilent 660, USA). The samples for this were prepared by using KBr disc method with 2 mg of sample in 100 mg KBr and the IR

spectra were obtained.

The binding energies and the surface chemical states of the Ca-Ce mixed oxide nanocomposite surface were determined by X-ray photoelectron spectroscopy (XPS). X-ray photoelectron Spectroscopy (XPS) measurements were taken using a VG ESCALAB MKII spectrometer with a Mg K α X-ray source (1253.6 eV, 120 W) at a constant analyzer energy model.

2.4. Protein leakage assessment and dehydrogenase enzyme activity assay

Protein leakage studies were carried out as described previously [27]. The Ca-Ce NC concentration was set in the range of 5 – $100 \mu\text{g mL}^{-1}$ for each bacterial strain and the bacterial cell's concentration was kept at 10^6CFU mL^{-1} . The sample (1.0 mL) was obtained from each culture tube at an interval of 2 h and centrifuged for 5 min at 4°C . The supernatant was frozen at -20°C . This was followed by estimation of protein concentration by the Bradford assay [28].

Dehydrogenase enzyme activity was estimated using (3-(4,5-dimethylthiazol-2-yl)-2,5-diphenyltetrazolium bromide) tetrazolium (MTT) reduction method. MTT was dissolved in double distilled water (DDW) to have a concentration of 0.1mg mL^{-1} and stored at -20°C . MTT is a positively charged water-soluble yellow dye that instantly enters viable bacterial cells and reduces to water-insoluble purple formazan crystals by the dehydrogenase system of active cells. The reduction reaction was initiated by adding MTT to the Ca-Ce NC treated cell suspensions, and the mixtures were incubated at 37°C for 4 h within the open tube cap. The visual change was determined spectrophotometrically by measuring the absorbance of the extracted solution at 490 nm. Boiled bacterial cells comprising deactivated enzymes were negative controls (–ve). On the other hand, non-boiled bacterial cells with normal enzymatic activity were positive controls (+ve). The cell viability was estimated by MTT assay [29].

3. Results and discussion

3.1. BET and surface morphology analysis

The specific surface area is one of the most important quantities for characterizing novel porous materials. BET analysis was carried out for the specific surface area from nitrogen adsorption-desorption isotherms [30]. Specific surface area of Ca-Ce NC obtained was $349.9 \text{m}^2 \text{g}^{-1}$ where the plot of $1/[w(p/p_0) - 1]$ against p/p_0 is shown in Fig. S1. The Dubinin–Astakhov (D–A) plot illustrated pore size distribution and pore characteristics as shown in Fig. S1 inset (ESI file) [31]. D–A pore radius of the synthesized Ca-Ce NC was 15\AA . The high specific surface area and small pore size of the Ca-Ce NC are the key factors of higher antibacterial activity and very good fluoride removal efficiency.

The detailed surface morphology analysis of the synthesized Ca-Ce NC demonstrated that the particles of irregular sizes and shapes formed because of the aggregation of fine particles (Fig. S2a) with an average particle size of $\sim 7 \text{nm}$ calculated using Scherrer's formula in XRD analysis as shown in Fig. S2b (ESI file).

3.2. Antibacterial activity studies

The antibacterial activity of Ca-Ce mixed oxide NC was determined in terms of IC_{50} which is defined as the half maximal inhibitory concentration and is a measure of the effectiveness of a substance in inhibiting a specific biological or biochemical function. The IC_{50} ($\mu\text{g mL}^{-1}$) values were determined from the comparison of obtained data to those of standard antibiotic's data shown in Figs. S3 and S4 (ESI file). Student's *t*-test analysis presented $p < 0.05$ at a higher Ca-Ce NC concentration, indicating a noticeable difference from the control. The 31.5 and $27 \mu\text{g mL}^{-1}$ of Ca-Ce NC concentration inhibited 50% growth of *E. coli* and *S. aureus* bacteria, respectively. The Ca-Ce NC showed 28.6 and 29.5mm zone of inhibition (ZOI) against *E. coli* and *S. aureus*

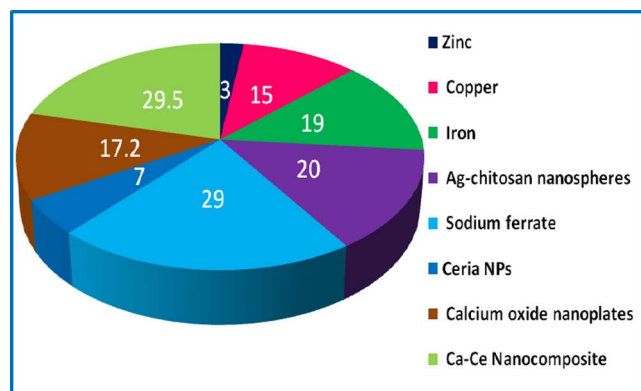


Fig. 1. Comparative zone of inhibition of Ca–Ce mixed oxide NC and reported different nanomaterials.

bacteria, respectively, which were quite comparable to those of ampicillin (30 mm). The results drawn from agar diffusion assay suggested Ca–Ce NC as an effective bactericide for both Gram-positive and Gram-negative bacteria (Fig. S5). Furthermore, the ZOI of Ca–Ce mixed oxide NC against *E. coli* and *S. aureus* bacteria was significantly higher than previously reported different materials as shown in Fig. 1 [17,18,29–34]. The effective bactericidal properties were due to enhanced membrane permeability and intracellular constituents' leakage caused by Ca–Ce NC resulting in severe damage and eventually cell death. This was further confirmed by membrane protein leakage and dehydrogenases enzyme activity studies.

3.3. Mechanism of antibacterial activity

The mechanism of action of Ca–Ce mixed oxide NC with bacteria was confirmed by scanning electron microscopy (SEM) analysis, membrane protein leakage studies, and dehydrogenase enzyme activity study as discussed in the following sections.

3.3.1. Nanocomposite's induced morphological changes in bacteria

The Ca–Ce NC's induced morphological changes in bacteria were investigated using SEM before and after its treatment. The fresh *E. coli* cells were having rod-like morphology and intact membrane (Fig. 2a) but after exposure to Ca–Ce mixed oxide NC it showed bursting of bacterial cells and shape changed to bulbous shape with the disintegrated membrane (Fig. 2b). Furthermore, membrane disintegration was confirmed by leakage of the cytoplasm of some bacterial cells (Fig. 2b). A similar observation was obtained in the case of *S. aureus* cells where its globules morphology (Fig. 2c) on treatment with Ca–Ce NC disintegrated to bulbous shape (Fig. 2d). Therefore, SEM analysis confirmed the role of the Ca–Ce NC in altering the morphology of bacterial cells that resulted in the death of the bacteria.

3.3.2. Effect of Ca–Ce NC on membrane protein leakage

To confirm the membrane disruption of bacterial cells, membrane protein leakage studies were performed. In a control experiment, initially $7.30 \mu\text{g mg}^{-1}$ of protein leakage occurred as compared to $8.88 \mu\text{g mg}^{-1}$ and $9.00 \mu\text{g mg}^{-1}$ protein leakage from Ca–Ce NC ($100 \mu\text{g mL}^{-1}$) treated with *E. coli* and *S. aureus* bacterial cells, respectively. However, the leaked amount of protein was $15.1 \mu\text{g mg}^{-1}$ and $15.5 \mu\text{g mg}^{-1}$ after 4 h of treatment of *E. coli* and *S. aureus* bacterial cells with Ca–Ce NC, respectively, while only $10.30 \mu\text{g mg}^{-1}$ protein leakage in control experiment was observed, indicated the role of the Ca–Ce NC in increasing the membrane permeability. Enhanced protein leakage through Gram-positive (*S. aureus*) bacterial cells compared to Gram-negative (*E. coli*) bacterial cells, suggested the higher antibacterial sensitivity of the *S. aureus* than the *E. coli*. Furthermore, the increase in Ca–Ce NC concentration resulted in enhanced cytoplasmic protein

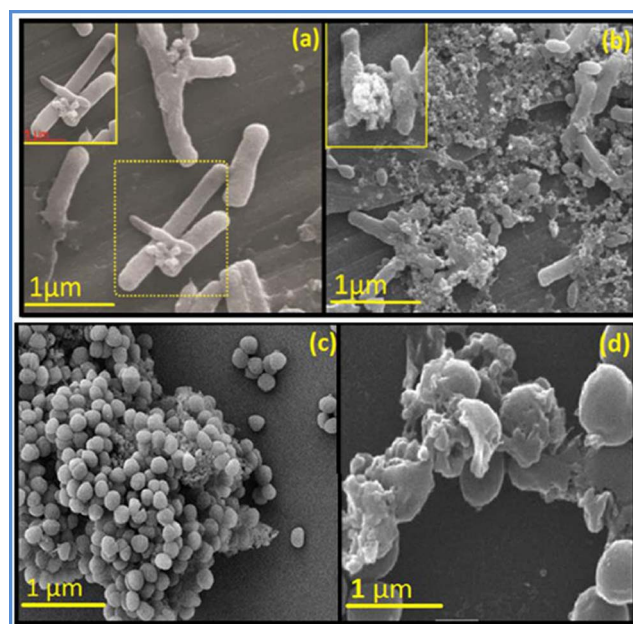


Fig. 2. SEM images of *E. coli* (a) before and (b) after incubation with Ca–Ce NC and *S. aureus* (c) before and (d) after incubation with Ca–Ce NC.

leakage, resulting in the death of the bacterial cell. The pictorial representation of this mechanism is shown in Fig. 3. Differential bacterial susceptibility may be because of structural and compositional variations in the Gram-positive and the Gram-negative bacteria cell membrane. The Gram-negative cell membrane has been found to have dynamic lipopolysaccharides O-side chains that are absent in Gram-positive cell walls. These rapidly moving side chains in *E. coli* bacteria may disable the formation of a metal-ion salt bridge, thus preventing the antibacterial effect at low Ca–Ce NC concentration.

3.3.3. Effect of Ca–Ce NC on dehydrogenase enzyme activity

The effect of Ca–Ce NC on dehydrogenase enzyme activity was studied by dissolving formed formazan crystals in phosphate-buffered saline (PBS) and quantified spectrophotometrically, where concentration was directly related to the number of metabolically active cells. The reduction in enzymatic activity was found to be a function of Ca–Ce NC concentration and the effect was much higher with $100 \mu\text{g mL}^{-1}$ Ca–Ce NC concentration compared to *E. coli* and *S. aureus* bacterial cells (control +ve) as shown in (Fig. 4a & b). Hence, the results suggested that the Ca–Ce NC significantly inhibited dehydrogenase enzyme activity. Furthermore, the Ca–Ce NC showed more reduced enzymatic activity in case of Gram-positive *S. aureus* cells than Gram-negative *E. coli* cells (Fig. 4a & b). Gram-negative *E. coli* cells have negatively charged cellular membranes and are a function of the isoelectric point (4–5). However, in the case of Gram-positive *S. aureus* cells, the membrane isoelectric point reached 7.0 ± 0.4 , resulting in the development of more negative charge on the surface in the culture medium [35,36]. As a result, the negatively charged *E. coli* cellular membranes at pH 7 showed higher resistance against the direct exposure to Ca–Ce NC (MOH_2^+ , $\text{pzc} = 5.0$, Fig. 5d inset) than *S. aureus* cells in aqueous suspensions at pH 7.

3.4. Optimization of Ca–Ce NC as nanoadsorbent

The effect of pH is quite significant for adsorption mechanism and an important parameter for the removal of fluoride from aqueous solution. Thus, the effect of pH on the removal of fluoride was studied in the range 3–12. The adsorption capacity gradually increased with increase in pH from 3 to 7, leveled off in pH range 7–10, and thereafter a significant reduction in adsorption capacity was observed (Fig. 5a). The

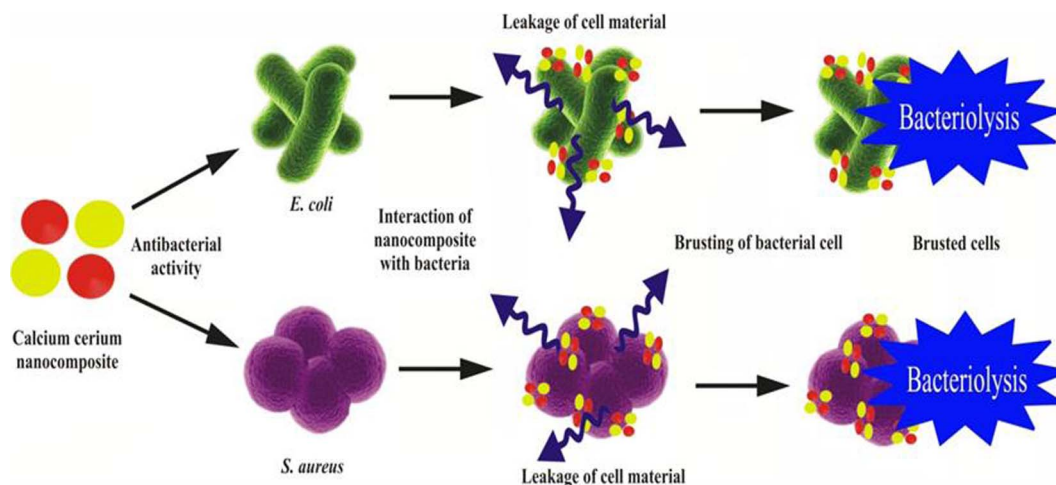


Fig. 3. Mechanism of action of Ca–Ce mixed oxide NC on bacterial cells.

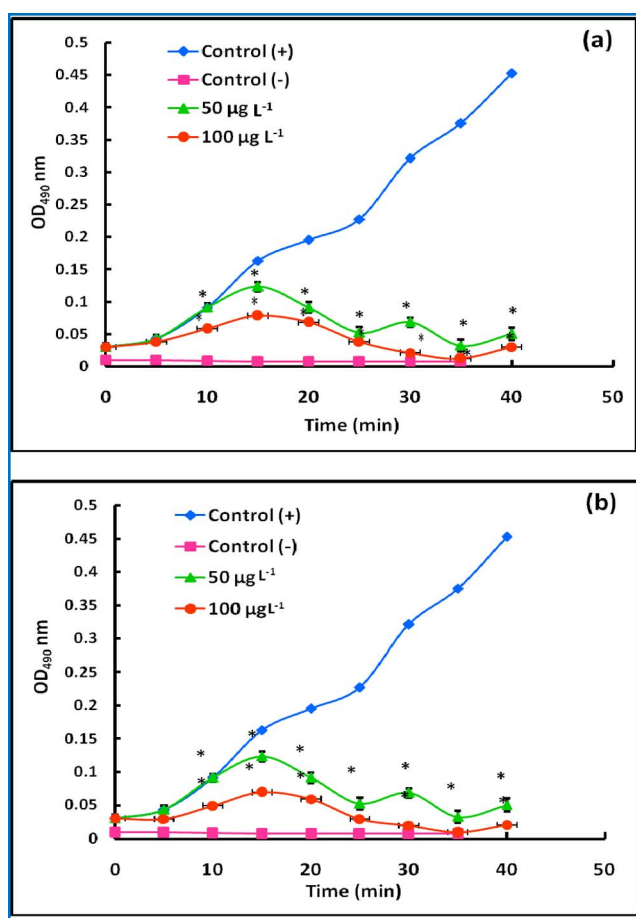


Fig. 4. Effect of Ca–Ce NC on dehydrogenase enzyme activity in (a) *E. coli* cells and (b) *S. aureus* cells compared to control.

solution pH controls the surface activeness and the electrostatic exchange reaction between fluoride and the surface of the Ca–Ce NC in solution. At lower pH, HF is formed due to the availability of more protons which is responsible for the poor fluoride adsorption. Furthermore, the fluoride adsorption was reduced in higher alkaline pH range due to the competition of OH⁻ ions with F⁻ ions for the similar adsorption active sites on Ca–Ce NC. Fig. 5d shows that the surface charge of Ca–Ce NC is pH dependent i.e. the surface charge arises from protonation or deprotonation of surface hydroxyl groups. This means

that only $\equiv MOH_2^+$ sites are available in acid media while $\equiv M^+$ sites are available if zeta potential is independent of pH. Thus, the electrostatic attraction takes place between positively charged surface hydroxyl groups and fluoride ions in acidic media and the ion exchange reaction occurs between the hydroxyl group of Ca–Ce NC and fluoride ions in basic media (8–10 pH). Therefore, the results demonstrated good adsorption capacity in the pH range 6–10.

The effect of variation of adsorbent doses on the fluoride uptake was analysed in the range of 1–200 mg L⁻¹ and the results are depicted in (Fig. 5b). The highest adsorption capacity (83.33 mg g⁻¹) was found at a Ca:Ce molar ratio of 1:3 showing synergistic effect as shown in Fig. 5b (inset). The increase in fluoride removal efficiency increased with Ca–Ce NC dose up to 120 mg L⁻¹ due to the availability of a greater number of active sites (Fig. 5b). Thereafter, only a marginal increase in fluoride removal occurred due to saturation of the surface sites.

The effect of initial fluoride concentration was studied in the range of 5–50 mg L⁻¹ and the results are presented in Fig. 5c. On increasing initial fluoride concentration, the fluoride removal decreased due to the availability of limited Ca–Ce NC surface sites than required for the high initial fluoride concentration (Fig. 5c).

3.5. Kinetic studies and effect of contact time

The kinetic studies demonstrated the applicability of pseudo second order kinetics model shown in Fig. S6 which supported chemisorption phenomenon involving the participation of valence forces among fluoride and Ca–Ce NC. The effect of the contact time on fluoride adsorption is shown in Fig. S6 (inset).

3.6. Effect of temperature and adsorption isotherms studies

Adsorption isotherms were studied at three different temperatures; 303, 313 and 312 K with initial fluoride concentration of 10 mg L⁻¹ and adsorbent dose of 0.03 g in 250 mL. The thermodynamic studies demonstrated that the fluoride adsorption phenomenon was endothermic (Table S2). The calculated thermodynamic parameters are shown in Table S3. The best fit isotherm was analyzed using R² values obtained from different isotherms showed that the adsorption followed the applicability order Freundlich > D–R > Langmuir isotherm (Table S4).

3.7. Regeneration, coexisting anions stability study

The economic viability of the Ca–Ce NC was checked by reusability studies in several cycles of the adsorption process. Firstly, the NC was subjected to the adsorption process at an initial fluoride ion

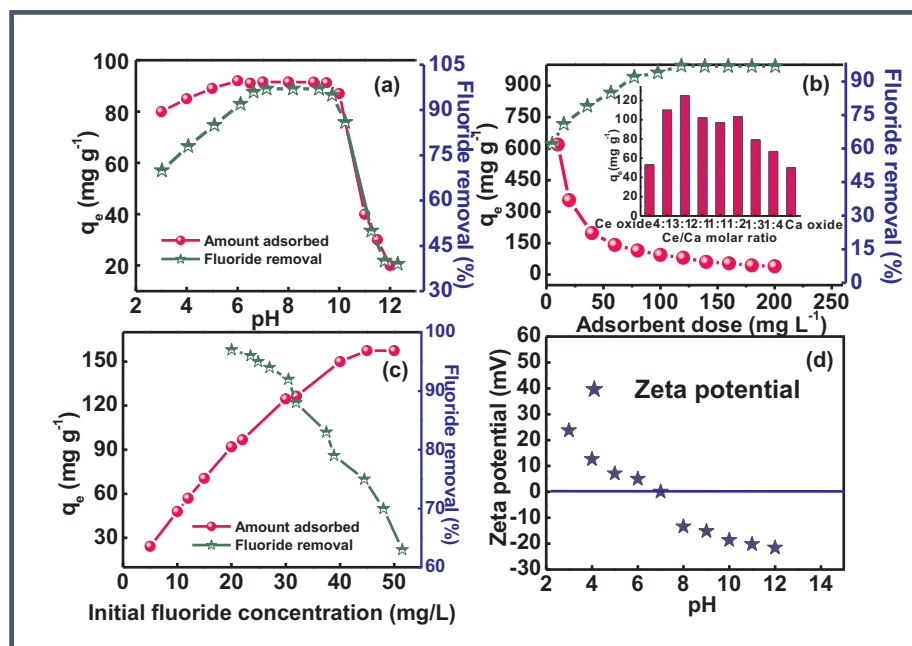


Fig. 5. Effect of (a) pH, (b) adsorbent dose, (c) initial fluoride concentration on adsorption capacity and (d) zeta potential study.

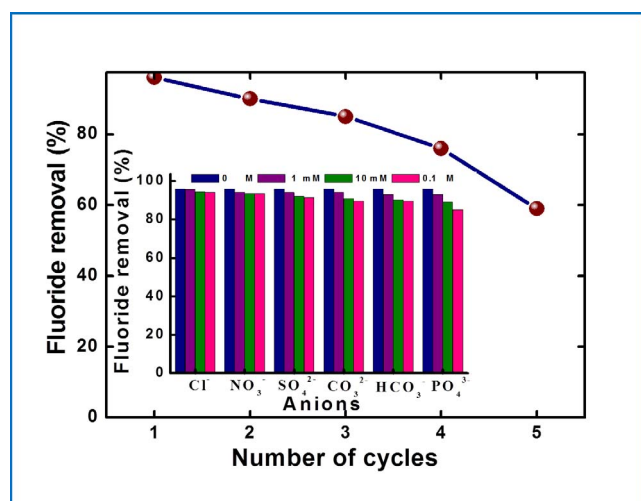


Fig. 6. Regeneration studies and coexisting anions effect on fluoride adsorption.

concentration of 10 mg L^{-1} , to examine the desorption efficiency of the adsorbent. The desorption processes were performed on the NC by using 0.1 M NaOH and re-activation was carried out using 0.1 M HCl . The Ca–Ce NC presented efficient reusability up to five cycles without significant loss in fluoride adsorption capacity (Fig. 6). The adsorption efficiency of the Ca–Ce NC was also studied in the presence of common coexisting anions: Cl^- , NO_3^- , SO_4^{2-} , CO_3^{2-} , HCO_3^- and PO_4^{3-} . The results showed that the fluoride removal efficiency of the Ca–Ce NC was negligibly affected in the presence of Cl^- , NO_3^- , SO_4^{2-} even at 100-times higher concentrations than fluoride ions. However, the fluoride removal efficiency was affected by the presence of CO_3^{2-} , HCO_3^- and PO_4^{3-} ions at high concentrations (Fig. 6). Therefore, the Ca–Ce NC showed excellent selectivity towards fluoride removal than several other adsorbents that have been utilized in environmental water samples [37–39].

The leach out studies were performed from filtrate after fluoride adsorption experiments using AAS analysis and the results demonstrated almost negligible concentrations of Ca and Ce metal ions than set by the Environmental Protection Agency (EPA). The five cycles reusability and negligible leakage of Ca and Ce ions make Ca–Ce NC an

efficient and robust adsorbent for field applications.

3.8. Mechanism of fluoride adsorption

It was imperative to evaluate the adsorption mechanism to understand the Ca–Ce NC characteristics and design the application part. The hydrolysis reaction occurs between the metal oxide and water that results in the development of surface hydroxyl groups on the metal oxide surface. The developed surface hydroxyl groups are considered as the main active sites for fluoride adsorption from the water. To confirm this, the Ca–Ce bimetal oxide NC was characterized by FTIR before and after fluoride adsorption. FTIR analysis supported inner-sphere mechanism of fluoride adsorption (Fig. 7a & b). The two sharp peaks at 1181.7 and 1043.7 cm^{-1} correspond to a metal hydroxyl group (M–OH) bending vibrations [39] (Fig. 7b). Both peaks disappeared upon fluoride adsorption which confirms the exchange of OH^- with the F^- ions. The peaks at 532.7 and 414.7 cm^{-1} correspond to Ce–O bond [40] and Ca–O bond [41] stretching vibration, respectively (Fig. 7a & b). After

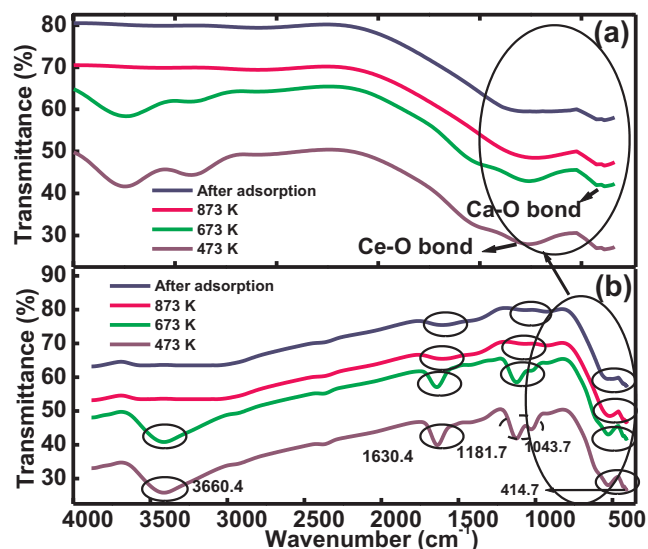


Fig. 7. FTIR spectra of Ca–Ce bimetal oxide NC before and after fluoride adsorption.

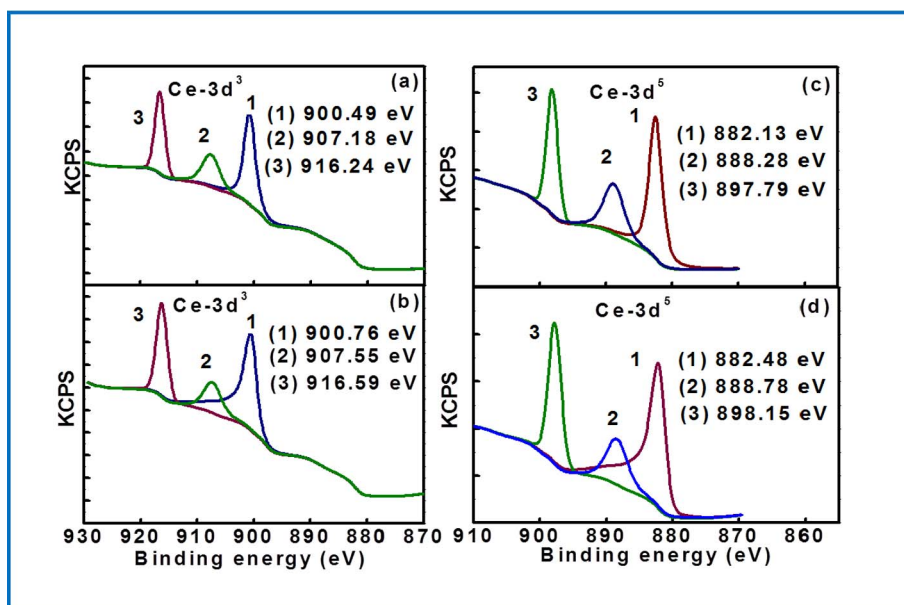


Fig. 8. XPS spectra of (a) cerium $3d^3$ before and (b) after fluoride adsorption and XPS spectra of (c) cerium $3d^5$ before and (d) after fluoride adsorption.

fluoride adsorption, the peaks shifted toward higher frequency supporting the inner-sphere complex mechanism of fluoride adsorption. It is apparent from the FTIR spectra (Fig. 7a & b) that the peak intensity of hydroxyl group at 1181.7 cm^{-1} and 1043.7 cm^{-1} diminished with increasing the calcination temperature (473–873 K) is due to the removal of surface hydroxyl groups which reduced adsorption capacity. Hence, adsorption experiments were carried out using adsorbent calcined at 473 K for maximum adsorption.

The qualitative, as well as quantitative molecular-level information on fluoride adsorption mechanism, was studied using the X-ray photoelectron spectroscopy (XPS) spectra as shown in (Fig. 8a & c) which demonstrated the presence of Ce(IV) as the major chemical state in the Ca–Ce NC. After fluoride adsorption, positive shifts in core levels were observed in these Ce 3d peaks as shown in (Fig. 8b & d) which indicated Ce–F covalent interactions, where electronegative fluoride atoms depleted the Ce 3d level's electron density. The shapes of Ca 2p peak

showed the positive shifts in binding energy values by $\approx 0.1\text{ eV}$ after fluoride adsorption (Fig. 9a & b) which is due to the replacement of $-\text{OH}$ group by the highest electronegative F^- ion (Table S6). Further, a reduction in the hydroxyl group peak intensity was noticed as shown in Fig. 9c & d) which is due to the exchange of OH^- ions with F^- ions. To confirm the distribution of fluoride on the Ca–Ce NC, a 50:50 Gaussian: Lorentzian peak shape was utilized to fit F1s spectra. The F1s spectra correspond to two different peaks that are Ca-bound fluoride (Ca–F) (684.5 eV), and Ce bound fluoride (Ce–F; 685.3 eV) (Fig. 9d). The comparative density of metal–F groups on the Ca–Ce NC was determined using the relative areas of the obtained subpeaks (Table S7). The results showed the involvement of $-\text{OH}$ groups of both in fluoride adsorption. However, the molar ratio of Ce–F (1.18 atomic%) was higher than Ca–F (0.84 atomic%) when Ce and Ca metal ions were present in 1:2 M ratio, confirmed the stronger affinity of Ce towards fluoride as compared to Ca. These discussions confirmed that the

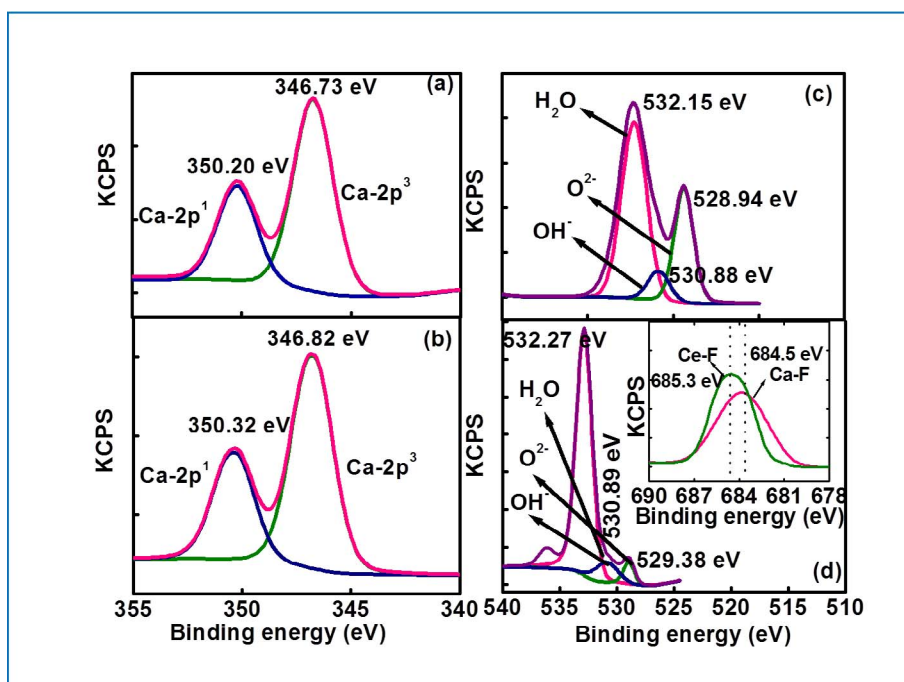


Fig. 9. XPS spectra of (a) calcium $2p^1$ before and (b) after fluoride adsorption and O1s spectra (c) before and (d) after fluoride adsorption, and F1s spectra of Ca–Ce nanocomposite at Ca: Ce molar ratio of 2:1((d) inset).

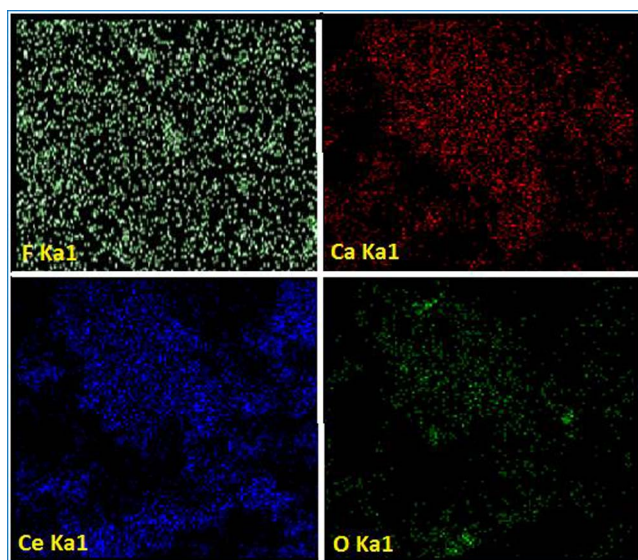


Fig. 10. Energy-dispersive X-ray spectroscopy (EDS) mapping after fluoride adsorption.

Table 1

The effect on values of different water analysis parameters before treatment and after treatment with Ca–Ce nanocomposite.

Parameter	Before treatment (mg L ⁻¹)	After treatment (mg L ⁻¹)
F ⁻	4.66	0.82
Cl ⁻	237.6	232.6
NO ₃ ⁻	39.0	37.0
SO ₄ ²⁻	200.4	197.4
CO ₃ ²⁻	195.2	185.2
HCO ₃ ⁻	218.0	208.0
PO ₄ ³⁻	257.0	243.0

surface reactions occurred on the Ca–Ce NC during fluoride adsorption was as follows:



The solution pH increased with fluoride concentration due to the release of OH⁻ ions upon fluoride adsorption according to Eq. (2). This was further verified by the equilibrium pH measurement of the solutions having different fluoride concentrations while the initial pH of the fluoride solutions was kept neutral (Table S8). The equilibrium fluoride solution pH increased from 4.32 to 5.99 with increasing initial fluoride concentration from 10 to 100 mg L⁻¹. To further investigate the binding of F⁻ ions by the adsorbent, energy dispersive X-ray spectroscopy (EDS) mapping of the adsorbent was performed after fluoride adsorption. EDS spectrum after fluoride adsorption showed evenly distributed fluoride on the Ca–Ce NC, adsorbent surface (Fig. 10), presenting direct adsorption of fluoride.

3.9. Field application

The potential field applicability of Ca–Ce NC (Ca:Ce ≈ 1:3) was tested for fluoride removal in environmental real water samples having high (4.66 mg L⁻¹) fluoride concentration; almost three times higher than the WHO standard limits (Table 1). The fluoride concentration was noted (0.82 mg L⁻¹) below the WHO limits after fluoride adsorption. A considerable amount of PO₄³⁻, CO₃²⁻ and HCO₃⁻ ions were also removed from the environmental water samples (Table 1). The reduction in the concentration of PO₄³⁻, CO₃²⁻, and HCO₃⁻ ions further demonstrated that these coexisting ions mainly compete with the fluoride ion for the same available active sites. These results presented the

suitability of treated water using presently proposed a method for potable purposes and the Ca–Ce NC can be efficiently utilized for the removal of fluoride from environmental water samples.

4. Conclusions

The present work demonstrated the mechanism for simultaneous antibacterial and fluoride removal by of Ca–Ce NC. The Ca–Ce NC presented good stability and high fluoride removal capacity (83.3 mg g⁻¹). The FTIR and XPS analyses confirmed that the metal hydroxyl groups contributed to the fluoride adsorption, where Ce–OH was found to be superior adsorption site even at low Ce in the nanocomposite as Ca:Ce ≈ 2:1. The reusability of the Ca–Ce NC with negligible leaching demonstrated its dual potential in bacterial and fluoride decontamination.

Acknowledgments

The authors gratefully acknowledge support from the Ministry of Science and Technology and Department of Science and Technology, Government of India under the scheme of Establishment of Women Technology Park, for providing the necessary financial support to carry out this study vide letter No, F. No SEED/WTP/063/2014. The author, S. Prasad is grateful to the University of the South Pacific, Suva, Fiji for support in various ways.

Conflict of Interest statement

We all the authors declare that there is not any ‘conflict of interest’ including any financial, personal or other relationships with other people or organizations.

Appendix A. Supplementary data

Supplementary data associated with this article can be found, in the online version, at <http://dx.doi.org/10.1016/j.cej.2017.12.030>.

References

- [1] M.G. McCormack, A.J. Smith, A.N. Akram, M. Jackson, D. Robertson, G. Edwards, *Staphylococcus aureus* and the oral cavity: An overlooked source of carriage and infection? *Am. J. Infect. Control* 43 (2015) 35–37.
- [2] M.M. Masadeh, S.F. Gharaibeh, K.H. Alzoubi, S.I. Al-Azzam, W.M. Obeidat, Antimicrobial activity of common mouthwash solutions on multidrug-resistance bacterial biofilms, *J. Clin. Med. Res.* 5 (2013) 389–394.
- [3] A.J. Smith, M.S. Jackson, J. Bagg, The ecology of *Staphylococcus species* in the oral cavity, *J. Med. Microbiol.* 50 (2001) 940–946.
- [4] P. Maurer, E. Hoffman, H. Mast, Bacterial meningitis after tooth extraction, *Br. Dent. J.* 206 (2009) 69–71.
- [5] D. Li, S. Zeng, M. He, A.Z. Gu, Water disinfection byproducts induce antibiotic resistance—role of environmental pollutants in resistance phenomena, *Environ. Sci. Technol.* 50 (2016) 3193–3201.
- [6] Z. Friedman, Antibiotic-resistant bacteria: prevalence in food and inactivation by food-compatible compounds and plant extracts, *J. Agric. Food Chem.* 63 (2015) 3805–3822.
- [7] S. Agnihotri, S. Mukherji, Immobilized silver nanoparticles enhance contact killing and show highest efficacy: elucidation of the mechanism of bactericidal action of silver, *Nanoscale* 5 (2013) 7328–7340.
- [8] P. Ghosh, B.G. Roy, S.K. Mukhopadhyay, P. Banerjee, Recognition of fluoride anions at low ppm level inside living cells and from fluorosis affected tooth and saliva samples, *RSC Adv.* 5 (2015) 27387–27392.
- [9] Z. Mandinic, M. Curcic, B. Antonijevic, M. Carevic, J. Mandic, D. Djukic-Cosic, C.P. Lekic, Fluoride in drinking water and dental fluorosis, *Sci. Total Environ.* 408 (2010) 3507–3512.
- [10] J. Li, Z. Hou, G.H. Chen, F. Li, Y. Zhou, X.Y. Xue, Z.P. Li, M. Jia, Z.D. Zhang, M.K. Li, X.X. Luo, Synthesis, antibacterial activities, and theoretical studies of dicoumarols, *Org. Biomol. Chem.* 12 (2014) 5528–5535.
- [11] L.Z. Wang, X.Q. Li, Y.S. An, 1,5-Benzodiazepine derivatives as potential antimicrobial agents: Design, synthesis, biological evaluation, and structure–activity relationships, *Org. Biomol. Chem.* 13 (2015) 5497–5509.
- [12] Y.W. Wang, A. Cao, Y. Jiang, X. Zhang, J.H. Liu, Y. Liu, H. Wang, Superior antibacterial activity of zinc oxide/graphene oxide composites originating from high zinc concentration localized around bacteria, *ACS Appl. Mater. Interfaces* 6 (2014) 2791–2798.

- [13] T. Jin, Y. He, Antibacterial activities of magnesium oxide (MgO) nanoparticles against food borne pathogens, *J. Nanopart. Res.* 13 (2011) 6877–6885.
- [14] C.P. Avanzato, J.M. Follieri, I.A. Banerjee, Biomimetic synthesis and antibacterial characteristics of magnesium oxide–germanium dioxide nanocomposite powders, *J. Compos. Mater.* 43 (2009) 897–910.
- [15] S. Cometa, R. Iatta, M.A. Ricci, C. Ferretti, E. de Giglio, Analytical characterization and antimicrobial properties of novel copper nanoparticles–loaded electro-synthesised hydrogel coatings, *J. Bioact. Compat. Polym.* 28 (2013) 508–522.
- [16] A. Roy, S.S. Gauri, M. Bhattacharya, J. Bhattacharya, Antimicrobial activity of CaO nanoparticles, *J. Biomed. Nanotechnol.* 9 (2013) 1570–1578.
- [17] K.S. Venkatesh, K. Gopinath, N.S. Palani, A. Arumugam, S.P. Jose, S.A. Bahadur, R. Ilangoan, Plant pathogenic fungus *F. solani* mediated biosynthesis of nanoceria: antibacterial and antibiofilm activity, *RSC Adv.* 6 (2016) 42720–42729.
- [18] G. Gedda, S. Pandey, Y.C. Lin, H.F. Wu, Antibacterial effect of calcium oxide nano-plates fabricated from shrimp shells, *Green Chem.* 17 (2015) 3276–3280.
- [19] W.X. Gong, J.H. Qu, R.P. Liu, H.C. Lan, Effect of aluminum fluoride complexation on fluoride removal by coagulation, *Colloids Interface Sci.* A 395 (2012) 88–93.
- [20] S. Meenakshi, N. Viswanathan, Identification of selective ion–exchange resin for fluoride sorption, *J. Colloid Interface Sci.* 308 (2007) 438–450.
- [21] I. Bejaoui, A. Mnif, B. Hamrouni, Influence of operating conditions on the retention of fluoride from water by nanofiltration, *Desalin. Water Treat.* 29 (2011) 39–46.
- [22] A. Dhillon, M. Nair, S.K. Bhargava, D. Kumar, Excellent fluoride decontamination and antibacterial efficacy of Fe–Ca–Zr hybrid metal oxide nanomaterial, *J. Colloid Interface Sci.* 457 (2015) 289–297.
- [23] T. Wu, L. Mao, H. Wang, Adsorption of fluoride on Mg/Fe layered double hydroxides material prepared via hydrothermal process, *RSC Adv.* 5 (2015) 23246–23254.
- [24] H. Cai, G. Chen, C. Peng, L. Xu, Z. Zhang, F. Ke, X. Wan, Enhanced fluoride removal by loading Al/Zr onto carboxymethyl starch sodium: synergistic interactions between Al and Zr, *RSC Adv.* 5 (2015) 101819–101825.
- [25] R. Devi, E. Alemayehu, V. Singh, A. Kumar, E. Mengistie, Removal of fluoride, arsenic and coliform bacteria by modified homemade filter media from drinking water, *Bioresour. Technol.* 99 (2008) 2269–2274.
- [26] X. Zhang, J. Qian, B. Pan, Fabrication of novel magnetic nanoparticles of multifunctionality for water decontamination, *Environ. Sci. Technol.* 50 (2016) 881–889.
- [27] M.R. Das, R.K. Sarma, S.C. Borah, R. Kumari, R. Saikia, A.B. Deshmukh, M.V. Shelke, P. Sengupta, S. Szunerits, R. Boukherroub, The synthesis of citrate–modified silver nanoparticles in an aqueous suspension of graphene oxide nanosheets and their antibacterial activity, *Colloids Surf. B Biointerfaces* 105 (2013) 128–136.
- [28] M.M. Bradford, A rapid and sensitive method for the quantitation of microgram quantities of protein utilizing the principle of protein–dye binding, *Anal. Biochem.* 72 (1976) 248–254.
- [29] P.K. Tandon, S.B. Singh, R.C. Shukla, Antimicrobial and oxidative properties of sodium ferrate for the combined removal of arsenic in drinking water with shell ash of unio, *Ind. Eng. Chem. Res.* 52 (2013) 17038–17046.
- [30] L.D. Hafshejani, S. Tangsir, E. Daneshvar, M. Maljanen, A. Lähde, J. Jokiniemi, M. Naushad, A. Bhatnagar, Optimization of fluoride removal from aqueous solution by Al₂O₃ nanoparticles, *J. Mol. Liquids* 238 (2017) 254–262.
- [31] A. Laybourn, J. Katrib, R.S. Ferrari-John, C.G. Morris, S. Yang, O. Udoudo, T.L. Easun, C. Dodds, N.R. Champness, S.W. Kingman, M. Schröder, Metal–organic frameworks in seconds via selective microwave heating, *J. Mater. Chem. A* 5 (2017) 7333–7338.
- [32] A. Dhillon, S.K. Soni, D. Kumar, Enhanced fluoride removal performance by Ce–Zn binary metal oxide: Adsorption characteristics and mechanism, *J. Fluorine Chem.* 199 (2017) 67–76.
- [33] A. Azam, A.S. Ahmed, M. Oves, M.S. Khan, S.S. Habib, A. Memic, Antimicrobial activity of metal oxide nanoparticles against Gram–positive and Gram–negative bacteria: A comparative study, *Int. J. Nanomed.* 7 (2012) 6003–6009.
- [34] P. Singh, J. Bajpai, A.K. Bajpai, R.B. Shrivastava, Removal of arsenic ions and bacteriological contamination from aqueous solutions using chitosan nanospheres, *Indian J. Chem. Technol.* 18 (2011) 403–413.
- [35] Y. Hong, D.G. Brown, Electrostatic behavior of the charge-regulated bacterial cell surface, *Langmuir* 24 (2008) 5003–5009.
- [36] K. Büttner, J. Bernhardt, C. Scharf, R. Schmid, U. Mäder, C. Eymann, H. Antelmann, A. Völker, U. Völker, M. Hecker, A comprehensive two–dimensional map of cytosolic proteins of *Bacillus subtilis*, *Electrophoresis* 22 (2001) 2908–2935.
- [37] C. Gao, X.Y. Yu, T. Luo, Y. Jia, B. Sun, J.H. Liu, Millimeter–sized Mg–Al–LDH nanoflake impregnated magnetic alginate beads (LDH–n–MABs): A novel bio–based sorbent for the removal of fluoride in water, *J. Mater. Chem. A* 2 (2014) 2119–2128.
- [38] Y.Q. Chen, Q.K. Zhang, L.B. Chen, H. Bai, L. Li, Basic aluminum sulfate@graphene hydrogel composites: Preparation and application for removal of fluoride, *J. Mater. Chem. A* 1 (2013) 13101–13110.
- [39] Y. Zhang, M. Yang, X.M. Dou, H. He, D.S. Wang, Arsenate adsorption on an Fe–Ce bimetal oxide adsorbent: Role of surface properties, *Environ. Sci. Technol.* 39 (2005) 7246–7253.
- [40] Y.H. Liu, J.C. Zuo, X.F. Ren, L. Yong, Synthesis and character of cerium oxide (CeO₂) nanoparticles by the precipitation method, *Metallurgija* 53 (2014) 463–465.
- [41] L. Fernández–Carrasco, D. Torrens–Martín, L.M. Morales, S. Martínez–Ramírez, *Infrared Spectroscopy in the Analysis of Building and Construction Materials*, “Infrared Spectroscopy–Materials Science, Engineering and Technology”, Book edited by Theophile Theophanides, ISBN 978–953–51–0537–4, Published: April 25, 2012.